

A digital twin system for thermal error compensation of numerical control machine tools based on multi-algorithm collaborative modeling

Qi Liu¹, Zhong Chen^{1,2*}[†], Qisen Wu³, Hao Wang¹, Xianmin Zhang^{1,2}

¹Shool of Mechanical and Automotive Engineering, South China University of Technology, Guangzhou, 510641,China.

²Guangdong Provincial Key Laboratory of Precision Equipment and Manufacturing Technology, South China University of Technology, Guangzhou, 510641,China.

³Jiesida Intelligent Technology (Guangdong) Co., Ltd., Foshan, 528312,China.

*Corresponding author(s). E-mail(s): mezhchen@scut.edu.cn;

[†]Q. Liu and Z. Chen contributed equally to this article.

Abstract

The precision degradation of machine tools is primarily caused by thermal effects generated during operation. Existing thermal error modeling methods rarely apply the physical mechanism of error formation in real-time error compensation. To address these limitations, a digital twin system for thermal error compensation of numerical control machine tools is proposed, built upon a multi-algorithm collaborative (M-AC) modeling framework. The system integrates a physical mechanism model (PMM) based on finite element analysis (FEA) and a data-driven model (DDM) utilizing a long short-term memory-convolutional neural network-attention architecture with a life-long learning approach (LL-LCA). This M-AC framework, paired with a dynamic reduced-order technique and heat-flow correction strategy, enables real-time thermal error prediction and compensation. Cutting experiments validate the system's effectiveness under varying conditions. For simple stepped workpieces, the average errors in the Y and Z directions were reduced by 85.09% and 76.23% respectively. For complex boss workpieces, the average errors in the Y and Z directions were reduced by 53.62% and 70.91%. These results demonstrate the effectiveness and robustness of the proposed system in improving machining accuracy.

Keywords: Digital twin, Reduced-order model, Thermal error compensation, Life-long learning, Multi-algorithm collaboration

1 Introduction

Thermal error is one of the primary factors affecting the machining precision of machine tools. During CNC machining, heat from the spindle, motor, and Z-axis lead screw propagates via conduction, producing non-uniform temperature fields, component distortion, and hence thermal error. Generally, there are two approaches to mitigate thermal error: error prevention and error compensation (Ni 1997). Error prevention involves improving design, precision manufacturing, and optimizing machine structure. However, for high-precision applications, this approach can lead to significantly increased costs. In contrast, error compensation is a more cost-effective and practical solution, involving the construction of accurate thermal error models, generating compensation values equal to the real errors, and feeding them into the machine-tool servo system to achieve error correction (Li et al. 2021).

Accurate thermal error modeling is crucial for effective compensation. With advancements in digital intelligence and big data, methods such as multivariable regression analysis (Zhang et al. 2016), neural network (Mize and Ziegert 2000), support vector machine (Miao et al. 2013), and hybrid model (Li et al. 2018) have been employed to develop thermal error models, achieving excellent results. With the improvement of parallel computing performance, deep neural networks

have demonstrated increasingly strong predictive capabilities, making their application in thermal error compensation more prevalent. Among deep learning methods, back-propagation (BP) and radial basis function (RBF) neural networks are commonly used for thermal error modeling (Li et al. 2021). BP networks are widely utilized due to their robustness and fault tolerance, with numerous studies optimizing their convergence speed and ability to escape local optima (Wang et al. 2020; Dai et al. 2024). Similarly, RBF networks, while known for fast convergence, are prone to local optima (de Farias et al. 2022; Tan et al. 2013). Compared to BP and RBF networks, recurrent neural networks (RNN) and their variants, such as long short-term memory (LSTM) network, gated recurrent unit (GRU), excel in learning the nonlinear features of time series (Yang and Ni 2005; Ma et al. 2023).

Despite these advancements, neural network-based thermal error modeling suffers from opacity, making it difficult to reflect the physical mechanisms underlying error formation. To address this, some researchers have integrated numerical methods with neural network (Fu et al. 2023; Liu et al. 2022b). While these methods capture physical mechanisms, they often struggle to adapt to complex and dynamic machining environments. To overcome this, researchers have proposed hybrid approaches, combining neural network and finite

element analysis (FEA) (Yi and Fan 2023). However, the lack of real-time performance in these approaches limits their application in thermal error compensation.

Digital twin technology offers a promising solution by enabling real-time interaction and feedback between physical and virtual spaces of machine tools. It facilitates knowledge accumulation, state monitoring, and feedback control, integrating geometric, data, and algorithm models for optimal performance (Liu et al. 2023; Niu et al. 2024). Many researchers in the field of thermal error studies have integrated their digital twins into their research and constructed thermal error models through deep learning, thereby promoting the advancement of thermal error compensation methods (Ma et al. 2023; Liu et al. 2021a). Some scholars have improved the digital twin method on this basis, by integrating spatial information into the neural network to achieve the capture of spatial features (Wu et al. 2024; Zhang et al. 2024). However, it failed to integrate the physical mechanisms, such as the principles of thermodynamics. Some scholars, in order to better reflect the physical mechanism, have adopted the method of combining the finite element model with the neural network to construct a digital twin system (Lu et al. 2022). Although the aforementioned digital twin methods incorporate models capable of predicting thermal errors and some also reflect

certain physical mechanisms, there is still a considerable gap from utilizing physical mechanisms in real-time and adaptively.

Building on these advancements, this paper aims to address the limitations of existing thermal error modeling methods and achieve accurate real-time thermal error prediction and compensation by leveraging a digital twin framework. The main contributions of this paper are as follows:

1. A life-long learning method based on elastic weight consolidation (EWC) is employed. Combined with a long short-term memory-convolutional neural network-attention (LSTM-CNN-Attention, LCA) architecture, the proposed data-driven thermal error model effectively prevents "catastrophic forgetting" under varying ambient temperatures.
2. A multi-algorithm collaborative (M-AC) modeling approach integrating physical mechanism model (PMM) and data-driven model (DDM) is developed. Finite element analysis (FEA) are constructed for the machine head, Z-axis ball screw, and machine-tool column. By dynamically correcting heat-flow inputs using real-time temperature data, the PMM is integrated with the neural network to reflect the thermal error's physical mechanism. To meet real-time requirements, a dynamic reduced-order model (ROM) is introduced to improve computational efficiency.

3. A digital twin system for thermal error compensation is designed. The system demonstrates effectiveness and robustness through cutting experiments on simple and complex workpieces under various working conditions.

The remainder of this paper is structured as follows: Related works are reviewed in Sect. 2. Sect. 3 outlines the proposed approach. Sect. 4 presents experimental validations and results. Finally, Sect. 5 concludes the paper, summarizing key contributions and suggesting future research directions.

2 Related works

RBF networks and BP networks are widely used in thermal error modeling. [de Farias et al. \(2022\)](#) applied RBF networks to thermal error modeling, while [Tan et al. \(2013\)](#) designed and trained a two-dimensional RBF network to model and estimate the geometric errors. On this foundation, [Feng et al. \(2023\)](#), [Fu et al. \(2019\)](#) and [Lu et al. \(2015\)](#) optimized RBF algorithms for enhanced thermal error modeling. [Wang et al. \(2020\)](#) and [Dai et al. \(2024\)](#) employed the BP network to predict thermal errors and achieved excellent results. In neural networks, RNN and its variants have demonstrated outstanding performance in time series modeling like thermal error prediction. For example, [Yang and Ni \(2005\)](#) applied integrated recurrent neural network (IRNN) to thermal error

modeling, effectively addressing non-stationary thermal elongation processes. [Ma et al. \(2023\)](#) proves the long-term memory of thermal error from theoretical and numerical analysis. LSTM, known for handling long-term dependencies, have also demonstrated superior performance in capturing thermal error dynamics ([Liu et al. 2021c,b](#); [Ngoc et al. 2022](#); [Li et al. 2024](#); [Liu et al. 2022a](#)). From this, it can be seen that RNN and LSTM neural networks still have significant room for improvement. How to optimize them to make them more suitable for the problem of thermal error prediction is worthy of further research.

For the issue of thermal errors, the most commonly used physical mechanism is the thermal physical mechanism. [Fu et al. \(2023\)](#) combined cubic exponential smoothing-unscented Kalman filtering (CES-UKF) and GRUs-based thermal error modeling, incorporating thermal hysteresis effects. Similarly, [Liu et al. \(2022b\)](#) developed thermal expansion error (TEE) and thermal drift error (TDE) models based on the friction heat generation, heat conduction, and heat convection theory, integrating them with digital twin methods for enhanced error prediction and compensation. The commonly used methods in thermal error research also include finite element thermal analysis to simulate the heat conduction and convection processes of structures such as the spindle and the lead screw, and to obtain the temperature distribution and thermal error results. For

example, [Yi and Fan \(2023\)](#) used BP neural network to modify thermal boundary conditions in FEA simulations, achieving robust and accurate results under varied spindle states. The finite element model comprehensively reflects the thermal physical mechanism, but its potential for thermal error compensation has not been fully exploited. The main reason for this is its poor real-time performance.

The digital twin method has provided a new opportunity for the research on thermal error compensation technology. [Liu et al. \(2023\)](#) reviews the significant potential of the digital twin method in state monitoring and feedback control. [Liu et al. \(2021a\)](#) developed a digital twin system for thermal error control in large toothed grinders. [Ma et al. \(2023\)](#) proposed a self learning-empowered error control method based on digital twin, enabling real-time prediction and control. Similarly, [Niu et al. \(2024\)](#) proposed a digital twin system for cemented carbide cutting tool sintering, achieving a 98.9% manufacturing yield. Many scholars have achieved this by capturing the characteristics of temporal and spatial relationships, enabling the digital twin method to reflect physical relationships from a spatial perspective. [Wu et al. \(2024\)](#) conducted innovative research on deep learning networks, proposed the STIIN model, and constructed a digital twin system for thermal error compensation that significantly

enhances machining precision and system execution efficiency. [Zhang et al. \(2024\)](#) designed a digital twin system framework tailored for error control, which employs interactive fusion spatiotemporal graph convolutional network model to enable dynamic control and real-time monitoring of thermal errors. These novel models are specifically designed to capture the dynamic spatiotemporal dependencies inherent in thermal errors. However, it failed to integrate the physical mechanisms, such as the principles of thermodynamics. The temporal and spatial relationships described in the literature still have a considerable gap from the physical mechanism, and their explainability is also poor. [Lu et al. \(2022\)](#) introduced a hybrid model combining thermal elastic-plastic finite element (TEP-FEM) and the T-XGBoost algorithm to leverage time-varying digital twin characteristics. However, the essence of this method is still deep learning, and the data sources only come from the finite element model, without integrating actual data. Meanwhile, the mature technical parameters of the factory were utilized to verify the TEP-FEM model, but this lacked the real-time and adaptive application of the physical mechanisms.

Therefore, developing a real-time and effective digital twin system for thermal error compensation is of great significance. On one hand, data-driven models such as RNN and its variants still have considerable potential for optimization

in thermal error modeling and prediction. At the same time, finite element methods can provide assistance in thermal error modeling from the physical mechanism level, but their potential for real-time application in thermal error compensation has not been fully exploited. Therefore, how to integrate real-time and adaptive physical mechanisms with data-driven models is of practical significance, and digital twin technology can provide effective help.

3 Material and methods

3.1 Digital twin framework based on multi algorithm collaborative model

This paper designs the overall framework of the digital twin system for thermal error compensation (DTS-TEC). As shown in Fig. 1, the data utilized in the digital twin architecture originates from real machine tools, with multi-point temperature data acquired via temperature sensors and thermal displacement data collected through displacement sensors. Multi algorithm collaborative model (M-AC) is a combination of physical mechanism model (PMM) and data-driven model (DDM), playing a decisive role in DTS-TEC. For the PMM, the geometric model of the machine tool is discretized and subjected to finite element analysis (FEA). By analyzing the main heat

sources of the machine tool, the necessary boundary conditions for FEA are established, enabling simulations to obtain theoretical temperature and thermal error values under physical mechanisms. For the DDM, the datasets are constructed to train a deep learning model. Sensitive temperature points are selected from the multi-point temperature measurements, which, together with the thermal displacement data, constitute the training datasets. The trained deep learning model can then predict thermal errors in real time based on temperature inputs. The M-AC does not merely treat the PMM predictions as an extra data set; instead, it uses the information transferred from the PMM to the DDM to augment the physics-based, real-time, adaptive feature inputs. To construct it, dynamic reduced-order model (ROM) is applied to decrease the computational burden of finite element analysis. A data interface is established, allowing the PMM to receive real-time temperature data, which is then used to correct the heat flux in the reduced-order finite element model.

Finally, when the DTS-TEC is deployed on the shop floor, both the PMM and DDM utilize real-time temperature data to predict thermal errors, and a comprehensive thermal error prediction is ultimately generated. This predicted value is written into the machine tool's numerical control system to achieve real-time thermal error compensation. The M-AC can extract physical

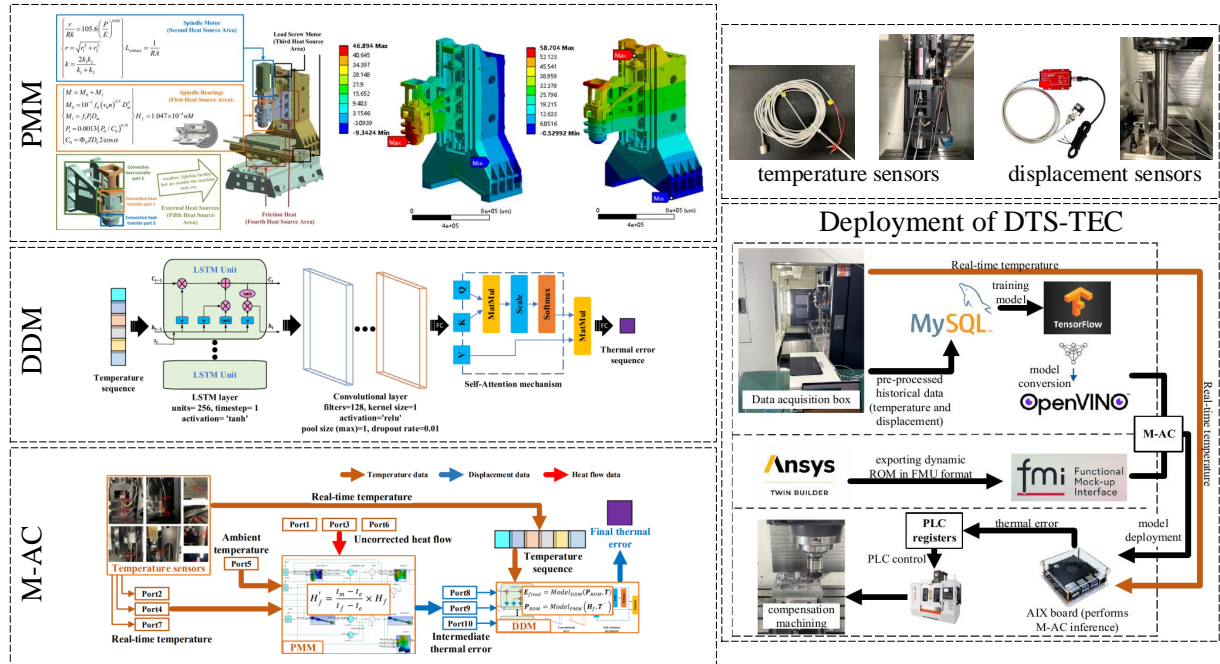


Fig. 1: Overall architecture of the DTS-TEC.

mechanism information that a single deep learning model cannot obtain from historical data, and it offers superior real-time adaptability compared to physics-based models previously used only for generating auxiliary datasets.

The specific steps of the proposed method are as follows:

- S1: Calculate finite element boundary conditions and perform finite element simulations of the machine tool under various operating conditions to obtain simulated temperature and displacement results.
- S2: Establish a dynamic ROM of the finite element model and develop a heat flux correction interface in Twin Builder to obtain the PMM.

S3: Deploy sensors to collect temperature and displacement data.

S4: Select sensitive temperature points from the collected data, construct datasets, and train a deep learning model to obtain the DDM.

S5: Combine PMM with DDM and use the datasets in S4 for training to achieve M-AC.

S6: Deploy the DTS-TEC on the machine tool, connect real-time temperature data, and write the calculated thermal error compensation values into the numerical control system of the machine tool, thereby enabling the digital twin architecture providing feedback control.

3.2 DTS-TEC implementation procedure

3.2.1 FEA boundary condition calculation

The research object is the BF-850V vertical linear rail milling machine (Hereinafter referred to as BF-850V), a widely used model in the machining industry. A figure of the BF-850V is shown in Fig. 2. The premise of boundary conditions calculation is the analysis of the heat source. Heat sources affecting the precision of BF-850V are categorized into five main areas:



Fig. 2: BF-850V vertical linear rail milling machine.

- i. Spindle Bearings (First Heat Source Area):
The angular contact ball bearings in the spindle generate heat due to friction between the balls and the inner/outer rings, significantly contributing to spindle thermal error.
- ii. Spindle Motor (Second Heat Source Area): The spindle motor, capable of reaching 12,000 rpm, generates substantial heat.

- iii. Lead Screw Motor (Third Heat Source Area):
The Z-axis lead screw motor generates heat to balance gravity, even under no-load conditions, leading to ball screw thermal expansion and spindle accuracy errors.
- iv. Friction Heat (Fourth Heat Source Area): Friction between components, such as lead screws, nuts, bearings, and guide rails, generates heat during machining under load.
- v. External Heat Sources (Fifth Heat Source Area): Environmental factors, such as ambient temperature, lighting, and external heat sources, influence the machine tool's temperature field and thermal error.

The accuracy and reliability of finite element analysis are significantly influenced by the thermal boundary conditions. Figure 3 shows the composition of the thermal boundary conditions of BF-850V, based on five heat source areas mentioned above.

The spindle's first heat source area is identified as the most critical contributor to spindle heating. H_f is the heat generated by bearing friction (Fan et al. 2018; Fan 2017). In its corresponding formula: M_0 and M_1 are the friction torques independent of load and dependent on load, respectively. f_0 is a factor related to lubrication, D_m is the bearing's mean diameter, v_0 is the lubricant's kinematic viscosity at operating temperature, P_1 is the equivalent bearing load, and

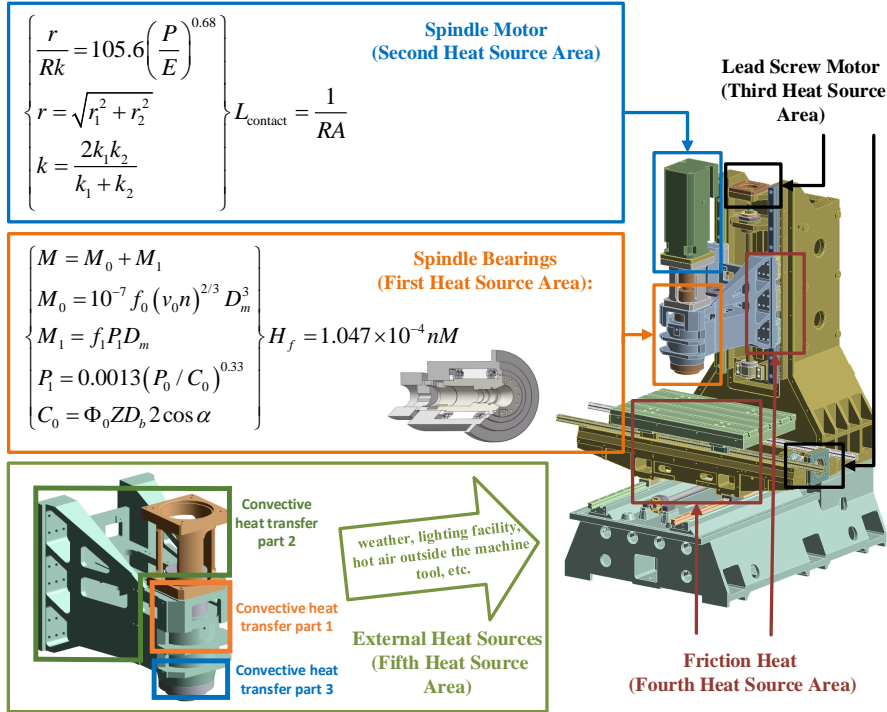


Fig. 3: Heat source analysis of the BF-850V.

f_1 is a parameter dependent on bearing type and load. For angular contact ball bearings, P_0 is the equivalent static load; C_0 is the basic rated load, Φ_0 represents the rated load factor, Z is the number of balls in the bearing, D_b is the diameter of the ball, α is the size of the contact angle.

The second heat source area involves heat transfer from the spindle motor to the motor base via the flange, leading to thermal deformation of the motor base. To better simulate the actual heat transfer process, the thermal resistance R between the two contact surfaces is calculated using the empirical formula (Fan et al. 2018; Fan 2017). P is the pressure of the contact surface, E is the

elastic modulus, k is the average thermal conductivity correction coefficient, and r is the root mean square of the roughness of the contact surface. r_1 and r_2 denote the surface roughness of the respective bonded surfaces, while k_1 and k_2 represent the thermal conductivity of these surfaces. ANSYS Workbench can simulate the heat transfer efficiency between two contacting surfaces by specifying their thermal conductivity values. The thermal conductivity is inversely proportional to thermal resistance, A is the area of contact surface.

For the third and fourth heat source areas, boundary conditions are simpler to calculate.

Since this machine has no load during data collection, no frictional heat is generated. The heat solely originates from the Z-axis lead screw motor.

In the fifth heat source area, heat loss occurs through thermal convection between the spindle's outer surface and the surrounding environment. Convection takes place in the following areas, as illustrated in the fifth heat source area of Fig. 3.

- i. Cooling device around the spindle sleeve: This area features a cooling groove surrounding the spindle sleeve. Coolant flows through the groove, providing the most significant heat dissipation.
- ii. Convex part of the spindle sleeve and headstock: This area, including the upper half of the spindle, is exposed to air, resulting in natural convection.
- iii. Front-end of the spindle: At high speeds, forced convection occurs between this area and the air due to spindle rotation.

3.2.2 Establishment of PMM

The finite element thermal analysis function of ANSYS Workbench is a crucial tool for analyzing and predicting machine-tool performance. By defining boundary conditions, structural and material parameters, the temperature field distribution of the machine tool can be numerically analyzed. Based on temperature analysis results, the thermal error of the machine tool is obtained.

The dynamic ROM function within ANSYS Twin-Builder is employed for reduction of the finite element simulation model, enabling the prediction of temperature and thermal error outputs under various input conditions with reduced computational expense. Figure 4 illustrates the process of constructing a dynamic ROM. The machine head, Z-axis lead screw, and machine-tool column in Workbench were subjected to simulations, with variable conditions. Each resultant "scenario" comprises two files: one for the excitation data required to build the ROM, named *Exc.csv*; and the other for the response data, named *Out.csv*. Furthermore, the simulated temperature points corresponds closely with the actual installation location of the temperature sensors, denoted as the temperature measurement points for heat-flow correction. Figure 5 delineates the location of these temperature measurement points. The simulated temperatures at these points serve as temperature responses for constructing ROM. Four heat-flow inputs are introduced for ROM construction. The excitation and response characteristics of the machine head, Z-axis ball screw, and machine-tool column across different "scenarios" are depicted in Fig. 6.

Input the heat-flow and other boundary conditions defined in the FEA model (Sect. 3.2.1), and append a set of auxiliary load cases that emulate temporal variations of the heat flow. The excitation-response pairs displayed in Fig. 6 serve

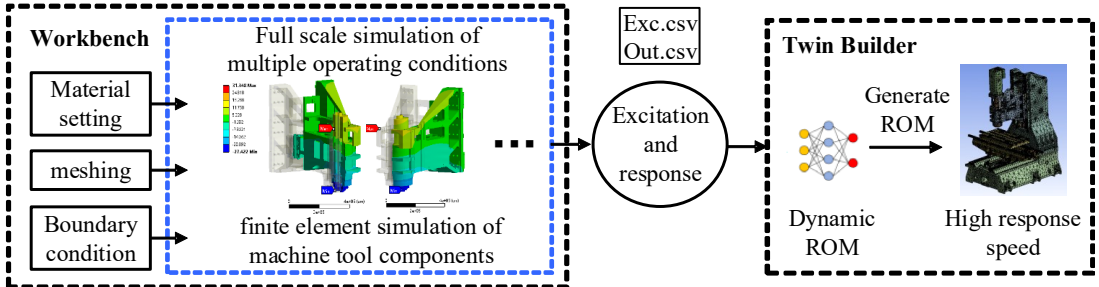


Fig. 4: The establishment process of a ROM.

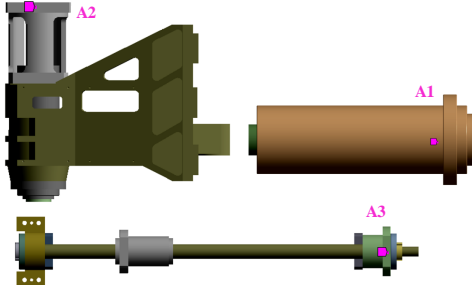


Fig. 5: The location of the temperature measurement points of A1, A2 and A3 for heat-flow correction.

twofold: they underpin the construction of the dynamic ROM and provide the reference data for the subsequent heat-flow correction scheme (Sect. 3.2.5). First, the “heat-flow excitation → temperature response” and “heat-flow excitation → thermal-error response” mappings supply the indispensable information for deriving the correction. Second, training the ROM under diversified heat-flow scenarios improves its generalisation capability and, consequently, the accuracy of the heat-flow correction.

3.2.3 Sensor deployment

Non-contact five-point method is used for measurement of thermal displacement. This method

involves positioning five measurement points along the centerline at the spindle’s end, arranged in a cross configuration, to gauge the relative displacement between the spindle and a stationary point on the worktable. The setup diagram for the five-point method on the vertical machining milling machine is depicted in Fig. 7, which primarily includes the eddy current displacement sensors, the sensor mounting fixture, the machine spindle, and the detection rod mounted on the spindle.

The temperature data is collected by PT100 temperature sensors installed on the machine tool, the actual installation diagram of the initial layout scheme of the temperature sensors is shown in Fig. 8. Table 1 describes the positions of labels in the figure.

3.2.4 Establishment of DDM

Selection of sensitive temperature points

An excessive number of temperature measurement points can negatively impact model performance. High collinearity among temperature sensors may

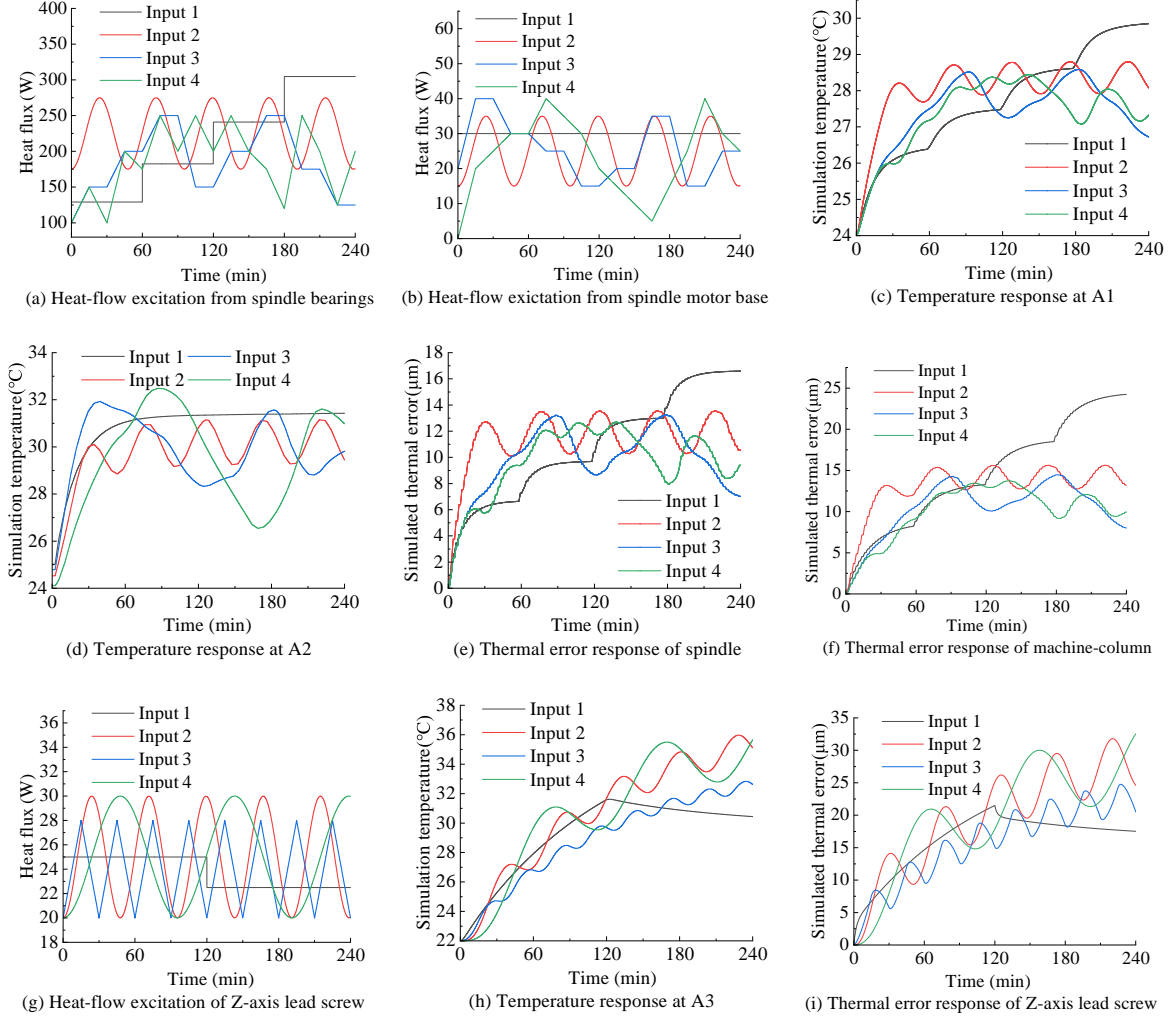


Fig. 6: Temperature responses and thermal errors of the machine head, Z-axis ball screw and machine-tool column under different heat-flow excitations: temperature responses T_h in (c) and (d) and thermal error response D_h in (e) are measured when machine-head heat-flow excitations H_h in (a) and (b) generate; temperature response T_z in (h) and thermal error response D_z in (i) when Z-axis ball screw heat-flow excitation H_z in (g) generates; thermal error response D_c in (f) when machine-tool column heat-flow excitation H_c happens on a hybrid thermal excitation combined from (a), (b), and (g).

interfere with model accuracy, while certain temperature signals might introduce noise, reducing prediction reliability. Selecting appropriate temperature points not only simplifies the model and shortens inference time but also minimizes collinearity errors, enhancing prediction accuracy.

This paper employs K -means clustering (Fu et al. 2021) combined with the gray correlation coefficient method (En-ming et al. 2014) to select the sensitive temperature points. The K -means clustering method divides temperature points into

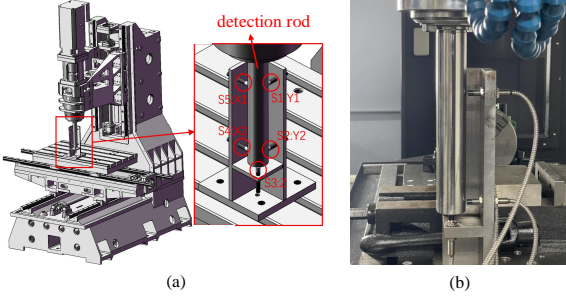


Fig. 7: Setup for the five-point method on a vertical machining-center mill. (a) Schematic of sensor layout: S_i denotes displacement sensor i ; $X1$ and $X2$ are the first and second X-direction sensors, respectively; remaining labels follow the same convention. (b) Photograph of the installed system.

Table 1: Temperature measurement point label and corresponding position in Fig. 8.

sensor label	position
T1 ¹ T2	Spindle front bearing
T3 T4	Between spindle's front and rear bearings
T5	Spindle rear bearing
T6 ²	Spindle motor flange
T7 ³	Z axis screw motor flange
T8	Inside wall of machine tool
T9	Machine table
T10	Inside wall of machine cooling box
T11	Ambient temperature

¹Equivalent to A1 in Fig. 5

²Equivalent to A2 in Fig. 5

³Equivalent to A3 in Fig. 5

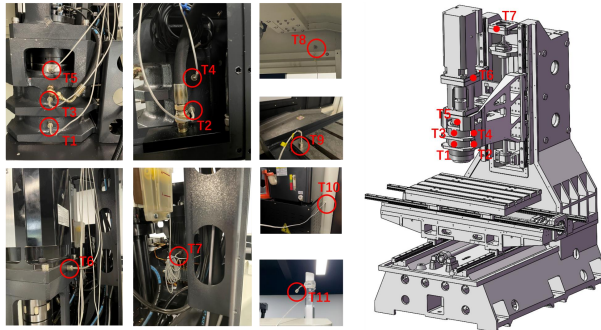


Fig. 8: Physical installation of the initial temperature-sensor layout (prior to selection of the sensitive points).

multiple groups by minimizing the sum of distances from each cluster center, and determines the optimal K value through contour coefficients. After obtaining the optimal grouping of temperature points, the work of grey correlation coefficient is to find out the most important temperature data point in each group, which depends on the degree of correlation between temperature data and displacement data. The temperature points

with higher degree of correlation is more suitable. The specific implementation of this method is shown in Algorithm 1.

LSTM-CNN-Attention network

Thermal errors often exhibit long-term accumulation effects, making it necessary to process long-sequence data effectively. Long short-term memory (LSTM) network, with their forget, input, and output gates, are well-suited for capturing temporal dependencies in thermal error data. To further enhance performance, this paper integrates convolutional neural network (CNN) and the attention mechanism (Fan et al. 2024) into the LSTM framework. CNN extracts deep features from temperature data, while the attention mechanism identifies key factors influencing thermal error. The resulting LSTM-CNN-Attention (LCA)

Algorithm 1 Selection of sensitive temperature points

Require: $T = \{t_i\}$ temperature data, $D = \{d_i\}$ displacement data, $[K_{\min}, K_{\max}]$

Ensure: Clusters $\{C_k\}$, Best points $\{p_k^*\}$

```

1:  $T_z \leftarrow \text{Z-score}(T); D_z \leftarrow \text{Z-score}(D)$                                 ▷ Normalize
2:  $K^* \leftarrow \arg \max_K \text{Silhouette}(K\text{-means}(T_z, K))$                          ▷ Optimal K
3:  $\{C_k\} \leftarrow K\text{-means}(T_z, K^*)$                                               ▷ Cluster temps
4: for each  $C_k$  do                                                               ▷ Select best per cluster
5:    $T_k \leftarrow \{t_i | t_i \in C_k\}$                                                  ▷ Relational coeff
6:    $\xi_i \leftarrow \text{GreyCoeff}(\text{Z-score}(T_k), D_z)$                                ▷ Best correlated point
7:    $p_k^* \leftarrow \arg \max_i \xi_i$ 
8: end for
  return  $\{C_k\}, \{p_k^*\}$ 

```

network efficiently handles one-dimensional time-series data such as temperature, and enhances sensitivity to factors that significantly affect thermal error. The network structure is shown in Fig. 9.

Life-long learning method based on elastic weight consolidation (EWC)

Life-long learning relies on the continuous updating of the LCA network, so temperature and displacement data under varying ambient temperatures are periodically input into the network for training. At this point, catastrophic forgetting often occurs, and the model's calculation accuracy for old data is poor. The cost of retraining the model or using all the data for training is unacceptable. Therefore, we introduce Elastic Weight Consolidation algorithm (EWC) (Liu et al. 2018), which identifies critical weights in the model and minimizes changes to these weights when adapting to new ambient temperature data, preventing catastrophic forgetting.

EWC achieves this by incorporating a regularization term into the loss function. Consequently, the key challenge lies in effectively representing the information content of the tasks encoded in the weights.

The Fisher information matrix serves as a measure of the likelihood function $p(x; \theta)$, quantifying the amount of information about the parameter θ . It is defined as the covariance matrix of the gradient of the logarithmic likelihood function. The gradient of the log-likelihood function indicates the flatness of the likelihood function's graph. A larger absolute value signifies a more pronounced "peak" in the graph, suggesting a greater amount of information contained in the observation at that point. Therefore, the gradient of the log-likelihood function is employed as the scoring function $s(\theta)$, which is expressed as:

$$s(\theta) = \frac{\partial \log p(x; \theta)}{\partial \theta} \quad (1)$$

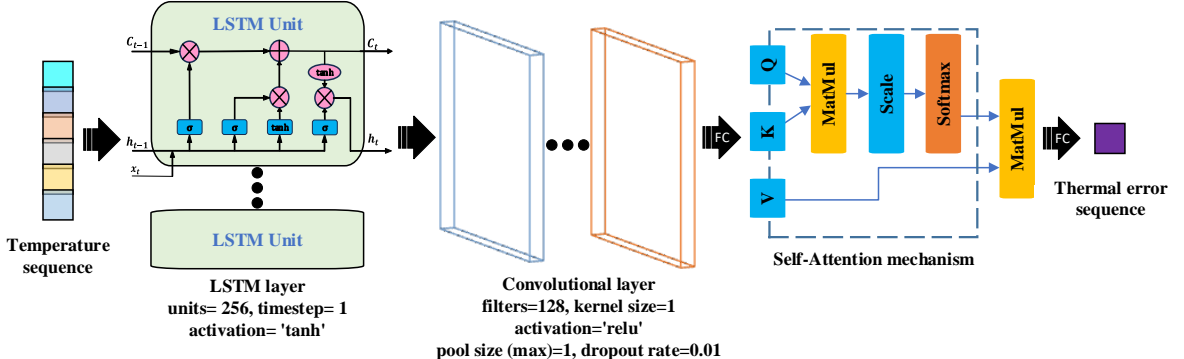


Fig. 9: LSTM-CNN-Attention (LCA) network structure diagram.

Then the Fisher information matrix is expressed as:

$$F(\theta) = E [s(\theta)s(\theta)^T] \quad (2)$$

Fisher information matrix serves as a measure of the information about old dataset carried by each weight parameter in LCA network. When the LCA network needs to be trained on a new dataset with different ambient temperature, the Fisher information matrix is introduced to build a new loss function. The hyperparameter λ is set to 0.01 by grid search and reflects the strength of the model's tendency to retain previous knowledge. The specific implementation process is shown in Algorithm 2.

3.2.5 Establishment of M-AC

It has been established that heat flux is directly proportional to the temperature increase of the machine tool (Fan et al. 2018). Consequently,

with a constant heat transfer area, heat flux can be corrected using the actual temperature data. Assuming that the measured temperature at the corrected temperature point is t_m , the temperature output of dynamic ROM is t_f , the ambient temperature is t_e , the heat flow before the correction is H_f , and the heat flow after the correction is H'_f , then H'_f can be expressed as:

$$H'_f = \frac{t_m - t_e}{t_f - t_e} \times H_f \quad (3)$$

Ports are established in TwinBuilder to facilitate communication between the ROM and external systems. After determining the heat inflow to calculate t_f , the ports read the real-time t_m from temperature sensors. It then employs Eq. (3) to perform real-time correction of the heat flow. The corrected heat flow yields the final thermal error output. Port1, Port3, and Port6 acquire the uncorrected heat flow calculated based on the machine's rotational speed. Meanwhile, Port2, Port4, Port5,

Algorithm 2 The implementation process of EWC algorithm

Require: Pre-trained model θ^* on Task 1, new Task 2 data, $\lambda = 0.01$

Ensure: Updated model θ retaining Task 1 knowledge

- 1: Compute Fisher info $\mathcal{F}_i = \mathbb{E}_{D_1}[\nabla_{\theta_i} \log p(y|\theta^*, x)^2]$
- 2: **for** each epoch on Task 2 **do**
- 3: **for** each batch $(x, y) \in D_2$ **do**
- 4: $\mathcal{L}_{\text{new}} = \mathcal{L}(\theta; x, y)$
- 5: $\mathcal{L}_{\text{ewc}} = \mathcal{L}_{\text{new}} + \frac{\lambda}{2} \sum_i \mathcal{F}_i (\theta_i - \theta_i^*)^2$
- 6: Update $\theta \leftarrow \theta - \eta \nabla_{\theta} \mathcal{L}_{\text{ewc}}$
- 7: **end for**
- 8: **end for**
- 9: **return** Updated model parameters θ

and Port7 respectively collect the actual temperature data from the corrected temperature points and ambient temperature: T1 on the spindle, T6 at the motor base, T11 for ambient temperature measurement, and T7 on the Z-axis screw flange. Port8, Port9, and Port10 are responsible for outputting the transient simulation thermal errors from the ROM.

The $Model_{DDM}(\cdot)$ function implements the LL-LCA architecture shown in Fig. 9, except that its input layer has been expanded. After the heat-flow correction, the output \mathbf{P}_{ROM} of the PMM model $Model_{PMM}(\cdot)$ and the temperature input \mathbf{T} are concatenated at the input layer and then fed into $Model_{DDM}(\cdot)$ to obtain the final thermal error \mathbf{E}_{final} , as expressed in Eq. (4).

$$\begin{aligned} \mathbf{E}_{final} &= Model_{DDM}(\mathbf{P}_{ROM}, \mathbf{T}) \\ \mathbf{P}_{ROM} &= Model_{PMM}(\mathbf{H}_f, \mathbf{T}') \end{aligned} \quad (4)$$

where \mathbf{T}' and \mathbf{T} denote the real-time temperature data from Port2, Port4, Port5, and Port7,

and the real-time temperature data at the sensitive points, respectively, and \mathbf{H}_f represents the uncorrected heat flow. The working principle of the multi-algorithm collaborative (M-AC) model is shown in Fig. 10.

3.2.6 Deployment of DTS-TEC

This paper uses specific software and hardware to implement the deployment of DTS-TEC. The dynamic ROM, exported in FMU format, is deployed in the programming environment to simulate thermal error behavior. LL-LCA uses pre-processed data stored in MySQL database for training, which is collected and stored through a specially built data acquisition box. To accelerate model inference, open visual inference neural network optimization (OpenVINO) is utilized, leveraging the hardware acceleration capabilities of the AIxBoard, a edge inference device for efficient forward calculations. The thermal error compensation values are transmitted to specified PLC

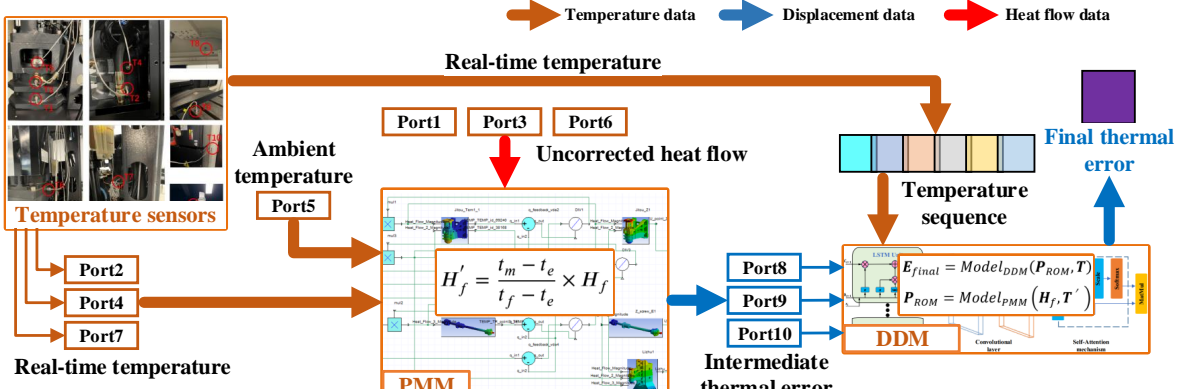


Fig. 10: The working principle of M-AC.

register of numerical control system by a communication program via TCP protocol. The BF-850V used in this study is equipped with Mitsubishi's M80 CNC. Within the Mitsubishi PLC register map, pairs R5700/R5701, R5702/R5703 and R5704/R5705 hold the real-time X-, Y- and Z-axis compensation values, respectively. The CNC applies these values instantaneously to offset the machine coordinate system. Figure 11 shows the deployment method of DTS-TEC.

The heat-flow rate in the second heat source area is estimated at 40 W. Calculations yield an estimated thermal resistance R_1 of $0.819\text{ K}\cdot\text{m}^2/\text{W}$ between the bearing outer ring and the spindle sleeve, R_2 of $0.269\text{ K}\cdot\text{m}^2/\text{W}$ between the bearing inner ring and the mandrel, and R_3 of $14.21\text{ K}\cdot\text{m}^2/\text{W}$ between the spindle sleeve and the headstock.

The convective heat transfer coefficients of the three convective heat transfer areas are set at $280\text{ W/m}^2\cdot\text{K}$, $25\text{ W/m}^2\cdot\text{K}$ and $100\text{ W/m}^2\cdot\text{K}$ respectively.

With the material information of the machine tool components established and the aforementioned boundary conditions for the spindle input into the finite element model, the transient simulation runs for one hour at each of the four speeds, under an ambient temperature of 24°C . The resultant temperature distribution across the machine head and the thermal error of the Z-axis are shown in Fig. 12 and Fig. 13.

4 Results

4.1 Analysis of the PMM

4.1.1 Finite element simulation result

The calorific value of the bearing at various speeds is computed in Table 2. There are two diagonal contact ball bearings on the spindle, and the friction heat is applied to the inner wall of the outer ring of the bearing.

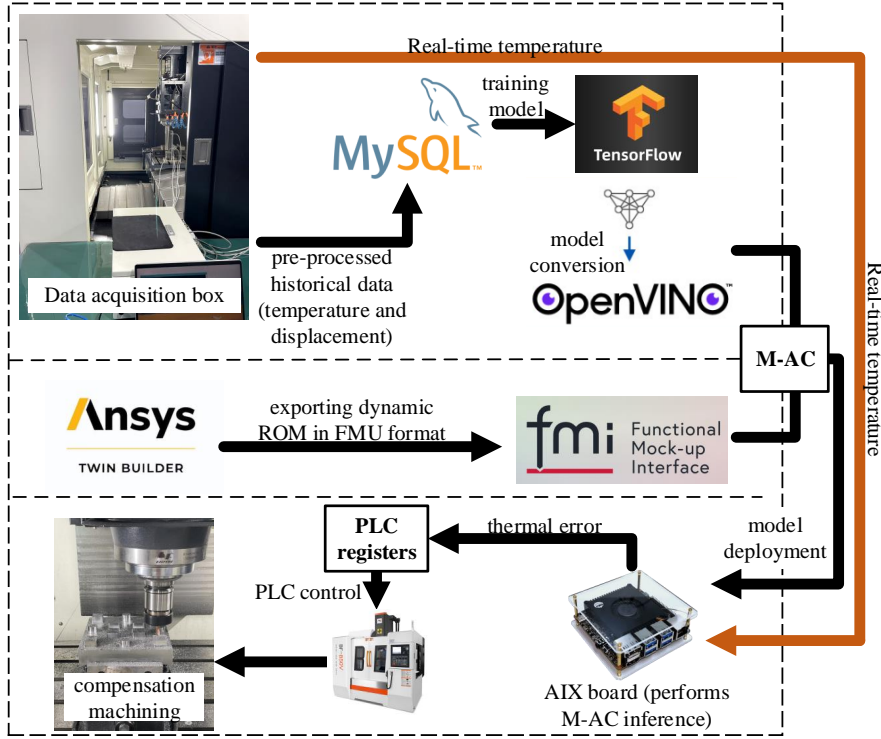


Fig. 11: Deployment method of DTS-TEC.

Table 2: Friction torque and calorific value of spindle bearing at different speed.

Spindle speed	Friction torque	Friction torque	Calorific value
n (r/min)	M_0 (N·mm)	M_1 (N·mm)	H_f (W)
5000	111.73	134.97	129.15
6500	133.08	134.97	182.43
8000	152.84	134.97	241.07
9500	171.39	134.97	304.73

The heat output of Z-axis screw motor is set at 20 W. Due to the absence of movement and free convection with air, the convective heat transfer coefficient of the Z-axis ball screw is lower than that of the spindle in contact with air, and is set at 25 W/m²·K. Assuming an ambient temperature of 22°C, the transient simulation runs for one hour at each of the four speeds. The temperature field

and thermal error of Z-axis ball screw are shown in Fig. 14 and Fig. 15.

The Z-direction accuracy of the end of the spindle is also affected by the machine-tool column. The heat source of the machine-tool column is not generated by itself, so it is necessary to combine the machine head, Z-axis ball screw and

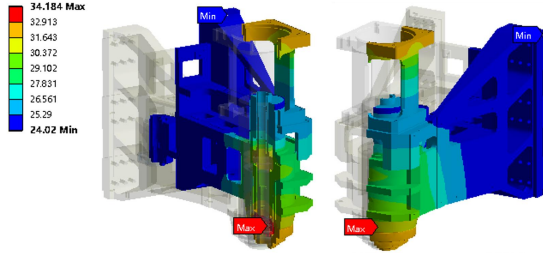


Fig. 12: Temperature field of machine head calculated by finite element model (unit: $^{\circ}\text{C}$).

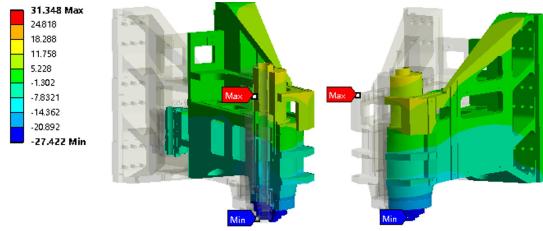


Fig. 13: Z-direction thermal error of machine head calculated by finite element model (unit: μm).



Fig. 15: Thermal error of Z-axis ball screw calculated by finite element model (unit: μm).



Fig. 14: Temperature field of Z-axis ball screw calculated by finite element model (unit: $^{\circ}\text{C}$).

machine-tool column together for the overall temperature field and thermal error simulation. The temperature field and thermal error of Y-axis and Z-axis are obtained, as shown in Fig. 16 and Fig. 17.

It can be seen that compared with the machine head thermal error simulation only, the overall thermal error is very different, which proves that

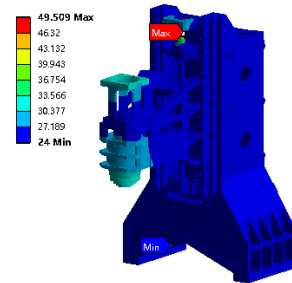


Fig. 16: Temperature field of machine-tool column calculated by finite element model (unit: $^{\circ}\text{C}$).

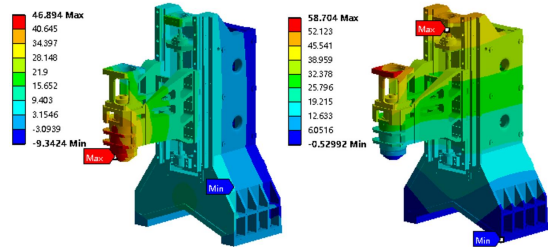


Fig. 17: Thermal error of Y and Z direction of machine-tool column calculated by finite element model (unit: μm).

the column has a important influence on the accuracy of the spindle end.

4.1.2 Comparison between full-order and reduced-order models

To assess the performance and adaptability of the ROM, the heat-flow excitation from the verification data set was fed into both the reduced-order model and the full-order model (finite element simulation). The temperature and thermal error output from each model were then compared, with the results presented in Fig. 18.

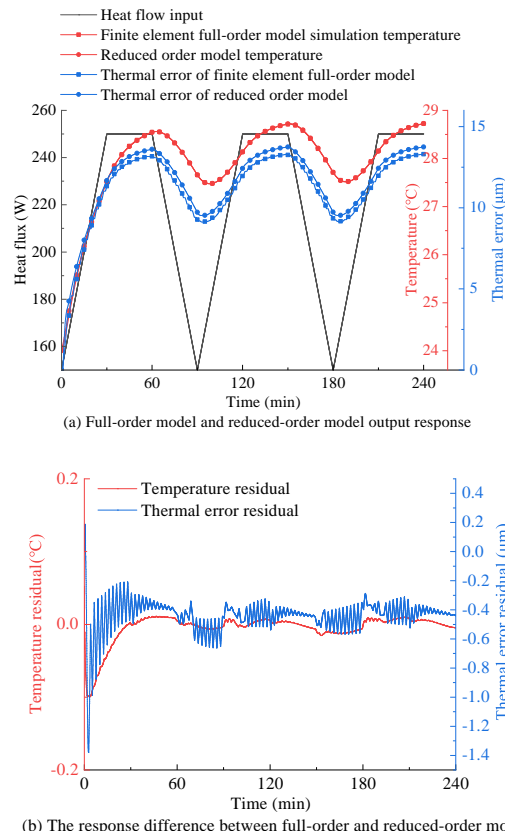


Fig. 18: Comparison of temperature and thermal error prediction results between reduced-order model and full-order model.

The reduced-order model yields temperature predictions whose residuals against the full-order model are negligible, and the thermal-error residuals remain within acceptable limits, confirming the ROM's predictive accuracy. Table 3 compares the time required to acquire temperature and thermal error output by the full-order model (finite element simulation) and the ROM. It is clear that the ROM substantially decreases simulation time and computational costs compared to the full-order model.

4.2 Analysis of the LCA network with life-long learning

4.2.1 Selection of sensitive temperature points

The clustering results of different K values and their contour coefficient are shown in Table 4.

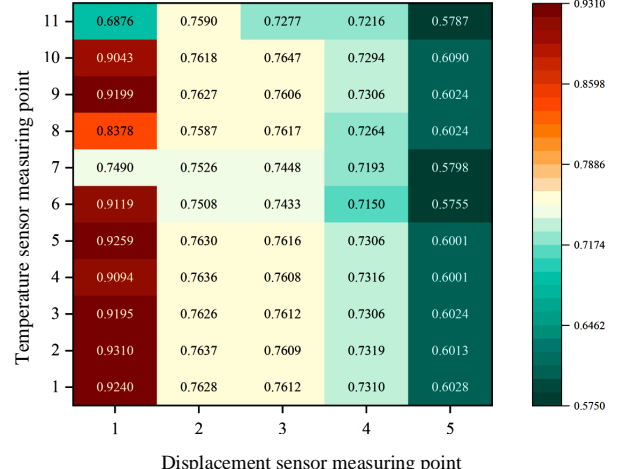


Fig. 19: The heat map of gray correlation coefficient between temperature data and thermal error data.

Table 3: Comparison of simulation calculation time between reduced-order model and full-order model.

Computational object	Full-order (s)	Reduced order (s)
Machine head temperature	456	1.71
Spindle thermal error	7564	2.36
Z-axis ball screw temperature	464	1.57
Z axis ball screw thermal error	6183	1.23
Machine-tool column temperature	276	1.46
Machine-tool column thermal error	7260	2.15

Table 4: Clustering results with different K values and their contour coefficients.

K	Clustering result	Contour coefficient
4	{ T1, T3, T5 }{ T2, T4, T8, T9, T10 }{ T6, T7 }{ T11 }	0.538
5	{ T1, T3, T5 }{ T2, T4, T9 }{ T6, T7 }{ T8, T10 }{ T11 }	0.527
6	{ T1, T3 }{ T2, T4, T9 }{ T5 }{ T6, T7 }{ T8, T10 }{ T11 }	0.523
7	{ T1, T3 }{ T2, T4, T9 }{ T5 }{ T6, T7 }{ T8 }{ T10 }{ T11 }	0.471
8	{ T1, T3 }{ T2 }{ T4, T9 }{ T5 }{ T6, T7 }{ T8 }{ T10 }{ T11 }	0.391

When $K = \{4, 5, 6\}$, the clustering performance is essentially equivalent and close to optimal. To balance feature diversity and engineering robustness, $K = 6$ was selected, yielding the following six measurement-point groups: Group 1: points 1 and 3; Group 2: points 2, 4, and 9; Group 3: point 5 (single); Group 4: points 6 and 7; Group 5: points 8 and 10; Group 6: point 11 (single).

The gray correlation coefficients between temperature data and thermal error data were computed and visualized in a heat map, as depicted in Fig. 19. The horizontal axis represents the displacement sensor, while the vertical axis corresponds to the temperature sensor.

The average gray correlation coefficient of each temperature measuring point was calculated, and its average gray correlation coefficient ψ_i was obtained. The results are shown in Table 5.

The identified temperature-sensitive points coincide with the six temperature measurement points fed into the data-driven model. The combination of temperature measurement points { T1, T2, T5, T7, T10, T11 } is the optimal set.

4.2.2 Analysis of the life-long learning method

To illustrate the lifelong-learning workflow, the LL-LCA network (with EWC) and its standard counterpart (without EWC) were sequentially trained on datasets D_1 , D_2 , and D_3 , each recorded at a different ambient temperature. The goodness-of-fit for thermal-error prediction on these datasets is plotted in Fig. 20. A fit degree of 1.0 indicates a perfect match, and the training data set is cycled every 1000 iterations.

Table 5: The average gray correlation coefficient of each temperature measuring point.

Point	1	2	3	4	5	6	7	8	9	10	11
ψ_i	0.756	0.758	0.755	0.756	0.753	0.702	0.709	0.738	0.755	0.754	0.695

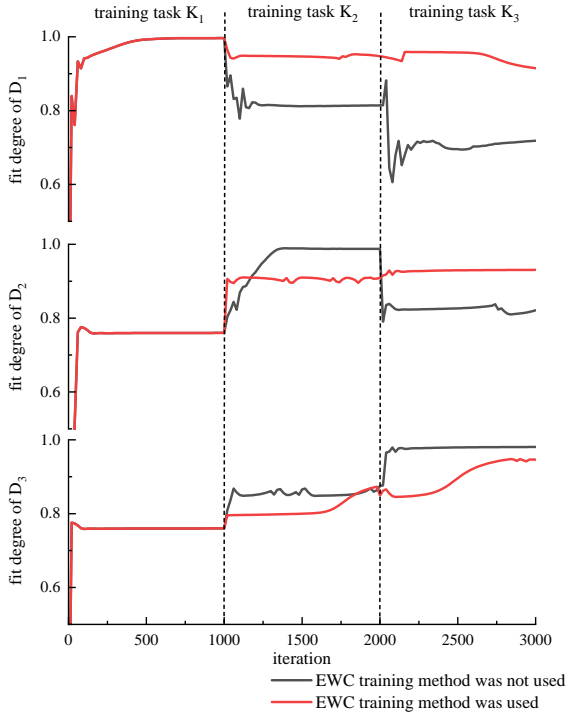


Fig. 20: Fit degree of thermal error prediction model to the three kinds of datasets during the training process.

It is observed that without the EWC method, the execution of training task K_1 significantly enhances the model’s fit on dataset D_1 , surpassing 98%. However, on datasets D_2 and D_3 , the model’s fit degree, while improved, remains below 80%. After switching to training task K_2 after 1000 iterations, the model’s fit on D_1 drops to

approximately 80%, indicative of significant catastrophic forgetting. Following another 1000 iterations, when the model shifts to task K_3 , its adaptability to D_1 further diminishes. At this time, most weight parameters crucial to D_1 , learned earlier by the model, are overwritten during training, while the fit degree for D_3 peaks. This training sequence highlights the catastrophic forgetting issue encountered by models without the EWC method during training across varying ambient temperatures, particularly impacting the model’s performance.

In contrast, with the EWC method, K_1 is trained for the initial 1000 iterations, and the model’s fit on each dataset matches that of the non-EWC training method. Upon reaching 1000 iterations, the training task transitions to K_2 , and the Fisher information matrix is leveraged to protect key information related to D_1 . The performance of model on D_1 drops slightly and remains at 94%. Due to the preservation of some weight parameters strongly linked to D_1 from update, the model’s performance on the second training on D_2 slightly decreases yet surpasses 90% compared to the second training without the EWC method. After another 1000 iterations, switching to task K_3 , the loss function is adjusted to prevent the

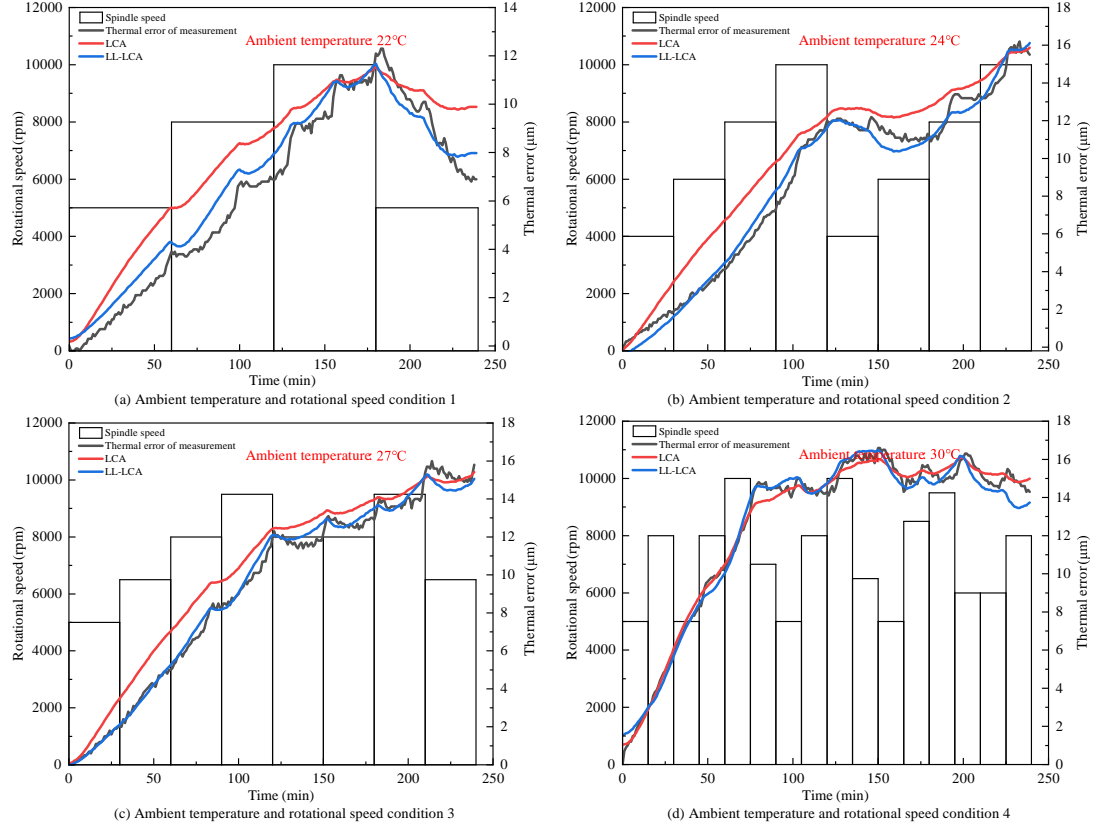


Fig. 21: Thermal error prediction results on the LCA network and LL-LCA network under different ambient temperatures and working conditions.

model from forgetting information about D_1 and D_2 . The model sustains a fit degree exceeding 90% across all three ambient temperature datasets, demonstrating that the life-long learning method effectively mitigates catastrophic forgetting.

4.2.3 Verification under a variety of operating conditions

The LL-LCA network (with EWC) and the standard LCA network (without EWC) were trained

under multiple ambient temperatures and operating scenarios, then evaluated on Y-axis thermal-error prediction. To emulate realistic roughing-to-finishing transitions, the spindle speed was deliberately varied during operation. The prediction results are shown in Fig. 21.

Under various conditions, the model exhibits slightly inferior prediction performance for measurement thermal error when devoid of the EWC method, with the maximum absolute error nearing $3 \mu\text{m}$. Conversely, employing the EWC method confines the maximum absolute error within $1 \mu\text{m}$.

4.3 Analysis of the M-AC

4.3.1 Effect of heat-flow correction

To verify the accuracy of the corrected ROM, a comparison was made between the measured temperature and the simulated temperature obtained after heat-flow correction at T7, as illustrated in Fig. 22. The measured temperature data was collected after the machine operated for four hours at speeds of 5000, 6500, 8000, and 9500 rpm, with the initial heat flow derived from previously mentioned heat-flow calculation formula. It is observed that the maximum difference between the measured and simulated temperatures is approximately 0.5°C , which proves the practical significance of the heat-flow correction method in enhancing the simulation precision of the heat transfer process.

4.3.2 Comparison with existing methods

The aforementioned efforts have built the M-AC model. A comparative experiment was conducted to predict thermal error in the Z direction at the spindle's end. The data set for this test is gathered under conditions where the machine tool's speed is gradually increased, with the temperature at each measurement point rising accordingly. To substantiate the high predictive accuracy of the M-AC model, several thermal error models, including the LL-LCA, M-AC, BP neural network

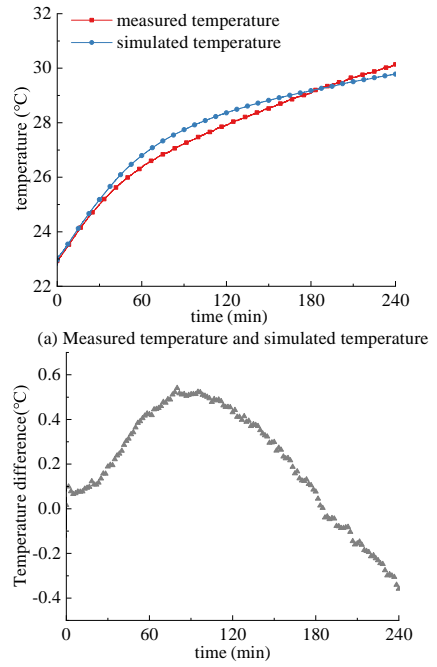


Fig. 22: Measured temperature and simulated temperature of T7 obtained after the heat-flow correction.

(Li et al. 2021), multiple linear regression (MLR) (Miao et al. 2013), and LSTM network (Liu et al. 2021c), were employed to model the Z-direction thermal error. Except for M-AC model, temperature sensitive points serve as input for the thermal error models. The learning rates for M-AC, LL-LCA, BP neural network, and LSTM network are all set to 0.0001, with Adam as the optimizer and identical training datasets. After identification, the regression coefficients for the MLR in the Z direction are as follows: $b_1=7.335$, $b_2=-7.923$, $b_3=-1.218$, $b_4=0.895$, $b_5=-0.221$, $b_6=1.745$. The MLR model for the Z direction is formulated as:

$$Z = 7.335T_1 - 7.923T_2 - 1.218T_5 + 0.895T_7 - 0.221T_{10} + 1.745T_{11} \quad (5)$$

Figure 23 shows the prediction and residual curves of the above thermal error models.

It is evident that all thermal error models are capable of predicting the general downward trend of thermal errors in the Z direction, but their predictive performances vary. The MLR model exhibits the poorest accuracy when dealing with the complex thermal errors in the Z direction. Except for the M-AC model, the predicted residuals tend to increase over time. Table 6 details the performance metrics of the prediction curves of thermal error.

As shown in the figure, the thermal error in the Z direction exhibits an "inflection point" distinct from temperature variations. The M-AC model has demonstrated superior predictive performance in both inflection point forecasting and overall accuracy. Before 14000 seconds, the LL-LCA outperformed other models, with lower predicted residuals compared to M-AC. However, beyond the inflection point, the predicted residual of LL-LCA sharply increases to approximately 6 μm , thus resulting in an overall performance inferior to M-AC. In contrast, M-AC maintains a maximum predictive residual of about 4 μm , significantly enhancing performance over a single LL-LCA network.

4.3.3 Evaluation on feasibility and real-time performance

The external-machine-coordinate compensation resolution of the test bench is 1 μm ; hence, the write frequency to the PLC register governs the compensation quality. Thermal-error growth is slow, whereas coordinate offset injection is virtually instantaneous, so the compensated tool path becomes a staircase whose step height equals the compensation interval. A long interval allows error to accumulate before a single 1 μm correction is applied, producing large steps that leave visible "cliff" marks on the finished surface and impose shock loads that shorten tool life. Consequently, the adopted strategy writes a 1 μm offset to the PLC register as soon as the predicted thermal error reaches that threshold. The dominant source of residual delay is the inference latency of the deployed model. To quantify this, 4 hours of temperature data (sampled at 1 Hz) were fed to the model five times, and the per-inference latency was recorded for five deployment scenarios: FMU only, OpenVINO only, TensorFlow only, FMU + OpenVINO (total edge time), and FMU without OpenVINO (total edge time). The resulting mean and range are reported in Table 7.

Adopting OpenVINO accelerates the neural network inference from 2050 ms to 1150 ms versus native TensorFlow, a 44% reduction that confirms the framework's effectiveness. Processing

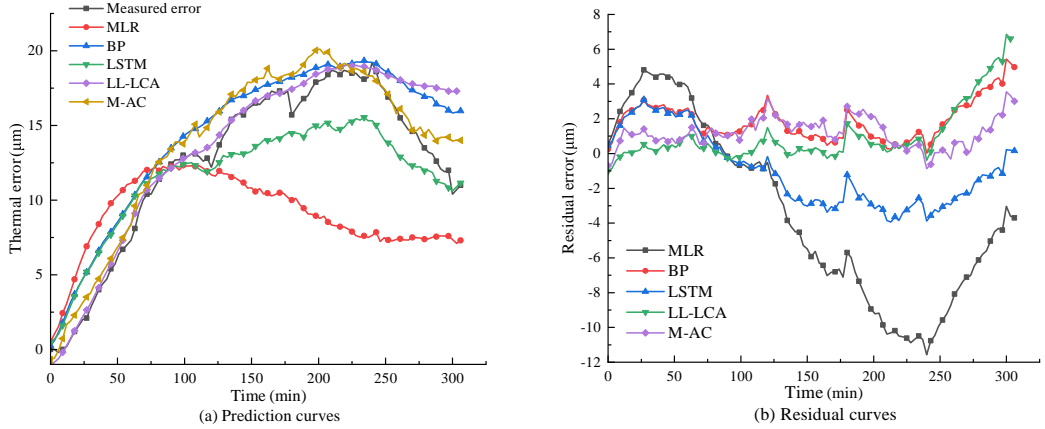


Fig. 23: Prediction and residual curves of multiple linear regression (MLR), BP neural network, LSTM network, LL-LCA network and M-AC.

Table 6: The performance metrics of different thermal error models.

Thermal error model	MSE	RMSE	MAE	Fitting degree (%)
MLR (Miao et al. 2013)	37.906	6.157	5.241	-
BP (Li et al. 2021)	5.834	2.415	2.080	78.5
LSTM (Liu et al. 2021c)	5.347	2.312	2.071	81.8
LL-LCA	3.851	1.962	1.119	86.9
M-AC	1.685	1.298	1.070	92.7

one temperature sample consumes only 0.443 ms, so the complete pipeline easily meets the real-time demands of thermal-error compensation.

with thermal-error compensation, one without. Tool: tungsten-carbide end-mill; ambient 17°C; spindle 3000 rpm (roughing) / 8000 rpm (finishing).

4.4 Cutting experiment

4.4.1 First experiment: simple stepped workpiece

In order to verify the compensation accuracy and robustness of the digital twin system, two groups of cutting experiments were conducted.

- Aluminium-alloy stepped workpieces** (identical geometry): one part machined

- A3-steel stepped workpieces** (same geometry): again, one with compensation, one without. Tool: tungsten-carbide; ambient 25°C; spindle 1500 rpm (roughing) / 5000 rpm (finishing); reduced cutting depth and feed rate.

Each machining operation commenced once the machine had fully cooled, with a machining duration of approximately one hour, resulting in a cuboid step dimension of 50 × 50 × 20 mm. The

Table 7: The time consumption of each module on the AIxBoard.

	Fluctuation range of inference time (ms)	Average time of single-inference (ms)
FMU	3900~4200	0.364
OpenVINO	1100~1200	0.079
FMU+OpenVINO	5000~5400	0.443
TensorFlow	2000~2100	0.145
FMU+TensorFlow	5900~6300	0.509

LL-LCA model was utilized for X-, Y-, and Z-axis compensation tasks.

To validate the compensation effect, various measuring points were established on the machined workpieces, and the workpiece dimensions were measured using a micrometer and compared against the theoretical machining dimensions. Figure 24 displays machined workpieces along with their measuring points.

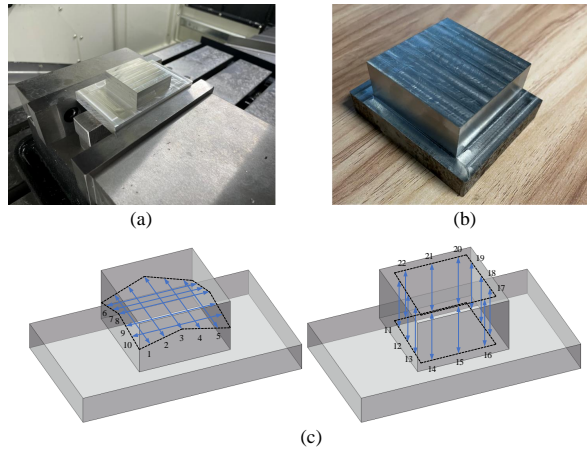


Fig. 24: Machined workpieces and measurement points. (a): Aluminium alloy workpiece. (b): A3 steel workpiece. (c): Measurement points from 1 to 22.

Of the 22 measuring points, the points numbered 1 to 10 are used to measure the length

and width of steps, located at different heights to evaluate surface smoothness. The subsequent 12 points, numbered from 11 to 22, are specifically allocated for measuring the step heights. These points are symmetrically distributed around the steps to mitigate the impact of random errors.

4.4.2 Second experiment: complex boss workpiece

To further validate the generalization and robustness of LL-LCA network and M-AC, the complex workpieces were machined: 12 small cylindrical and square bosses were machined from a $200 \times 200 \times 70$ mm blank. The workpiece material was die steel, with an ambient temperature of 30°C during machining. The outline is roughed out in advance, and each subsequent machining process is a roughing and finishing step based on this outline. The machining duration was 3 hours, with roughing at 2000 rpm and finishing at 6000 rpm. The machining errors in each direction when not compensate, the machining errors in each direction when the thermal error model is LL-LCA, and the machining errors in Z direction when the

thermal error model is M-AC will be measured. A coordinate measuring instrument, model FT-201210 with a maximum measurement error of $1.7 \mu\text{m}$, was employed to verify the compensation effect. The second workpiece processed is shown in Fig. 25.

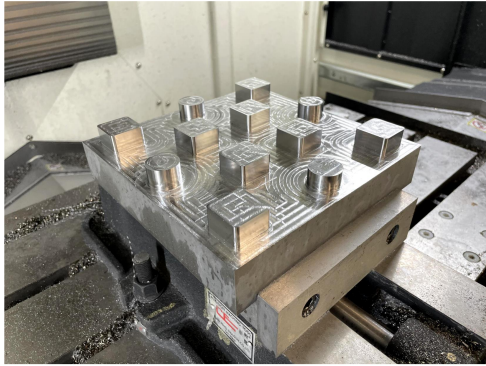


Fig. 25: The second complex workpiece processed.

With each machining operation, the procedure commences with roughing the bottom surface, proceeding then to fine milling, and subsequently to the fine milling of each small convex feature; once the axial surface milling is completed, the convex surface is planed. Figure 26 shows the processing sequence of the bosses.

4.4.3 Result of cutting experiment

The measurement results of each measuring point of the simple stepped workpieces are depicted in Fig. 27, in which the machining errors in length (X), width (Y), and height (Z) are marked in red, black and blue, respectively. Due to minimal error in the X direction, the discrepancies at points 6

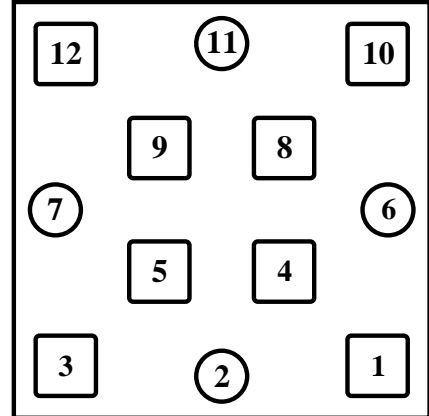


Fig. 26: The processing sequence of the second workpiece, where the numerical value assigned to each zone indicates its corresponding processing order.

to 10 are relatively minor. The workpiece without thermal error compensation exhibits machining errors exceeding $10 \mu\text{m}$ at points 1 to 5 and 11 to 22. Conversely, the workpieces with thermal error compensation effectively kept the machining error below $10 \mu\text{m}$, with machining errors from points 1 to 10 controlled beneath $5 \mu\text{m}$. The initial average machining errors in the Y direction and Z direction are $19.40 \mu\text{m}$ and $16.42 \mu\text{m}$ for the first group; for the second group, they are $13.00 \mu\text{m}$ and $16.58 \mu\text{m}$. After compensation, these errors are reduced to $2.80 \mu\text{m}$ and $5.08 \mu\text{m}$ for the first group, and $2.00 \mu\text{m}$ and $2.75 \mu\text{m}$ for the second group. The machining error of the first group and the second group of workpieces after compensation was reduced by an average of 73.37% and 83.67%, respectively, demonstrating the robustness of the proposed method in thermal error compensation during actual cutting.

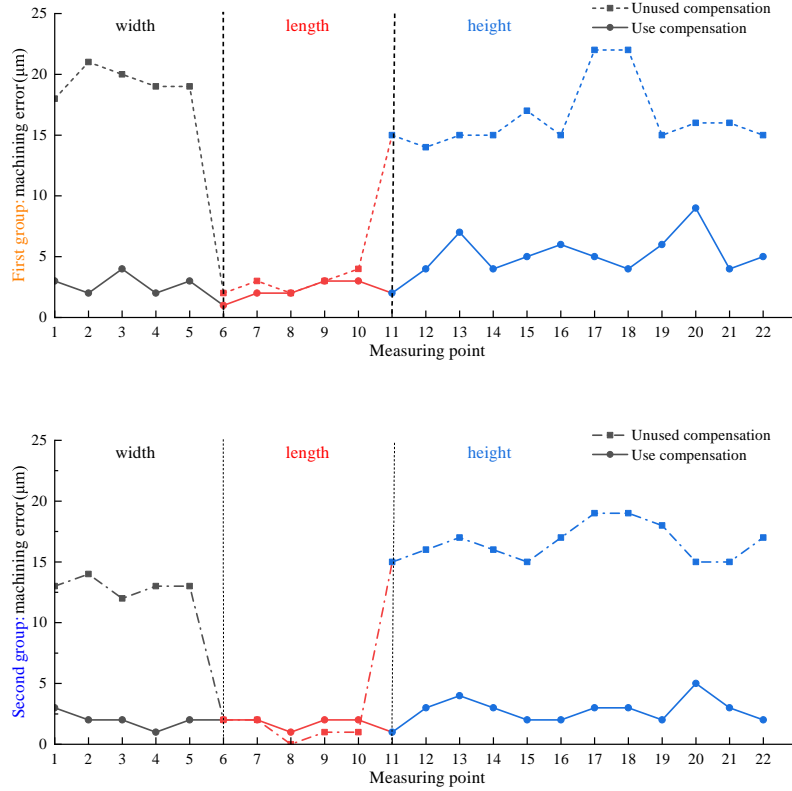


Fig. 27: The measurement results of each measuring point on the simple stepped workpieces.

Table 8: Measurement results of the second complex workpiece machined under different thermal error models.

Model	X (μm)			Y (μm)			Z (μm)		
	Max	Avg.	SD	Max	Avg.	SD	Max	Avg.	SD
Uncompen.	7.60	3.19	2.20	24.80	7.72	5.31	26.20	17.58	7.14
LL-LCA	-	-	-	8.70	3.58	2.13	13.40	7.23	3.98
M-AC	-	-	-	-	-	-	9.50	5.12	2.65

In the further experiment of complex boss workpiece, measurement results of the three experiments are shown in Fig. 29, Fig. 30 and Fig. 31. To better illustrate the relationship between machining errors before and after compensation, a point-line graph is plotted in Fig. 28.

The machining error in the X direction is small, so no compensation measures are implemented. The peak Y-direction machining error falls from $24.80 \mu\text{m}$ without compensation to $8.70 \mu\text{m}$ when the LL-LCA thermal-error model is active; the corresponding Z-direction error drops

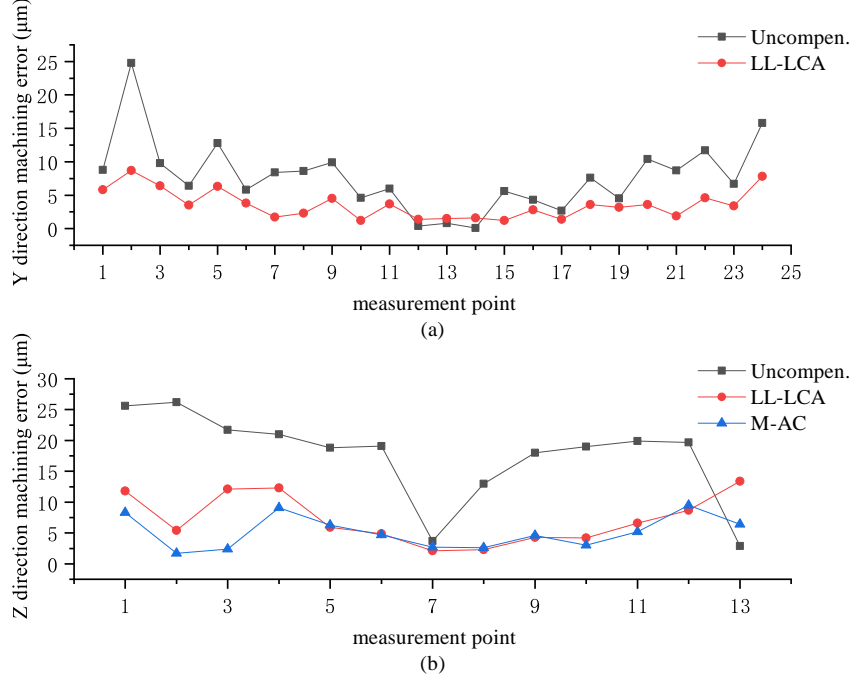


Fig. 28: The point-line graph illustrating the machining error of the complex boss workpieces. (a): machining errors in the Y direction without compensation and with LL-LCA compensation. (b) machining errors in the Z direction for uncompensated, LL-LCA compensation, and M-AC compensation.

from $26.20 \mu\text{m}$ to $13.40 \mu\text{m}$ with LL-LCA and to $9.50 \mu\text{m}$ with the M-AC model. The thermal error compensation results of different models are shown in Table 8, including the maximum value, average value and standard deviation (SD) of the absolute machining error.

Relative to the uncompensated case, the LL-LCA thermal-error model cuts the mean machining error by $4.14 \mu\text{m}$ in Y and $10.35 \mu\text{m}$ in Z, bringing the averages down to $3.58 \mu\text{m}$ and $7.23 \mu\text{m}$, respectively. Switching to the M-AC model for the Z-axis yields an additional $2.11 \mu\text{m}$ improvement, lowering the average Z-error to $5.12 \mu\text{m}$.

4.5 Discussion

- Figure 18 compares the temperature and thermal-error predictions of the ROM against those of the full-order model. For the prescribed heat-flow input, the ROM retains acceptable accuracy. We did not feed the full-order results into the M-AC module, because the finite-element solver is roughly three orders of magnitude slower than the ROM (Table 3), which would make the millions of training iterations required by the neural network impractical. Moreover, the ROM and the full-order model deliver identical outputs and interface with LL-LCA in exactly

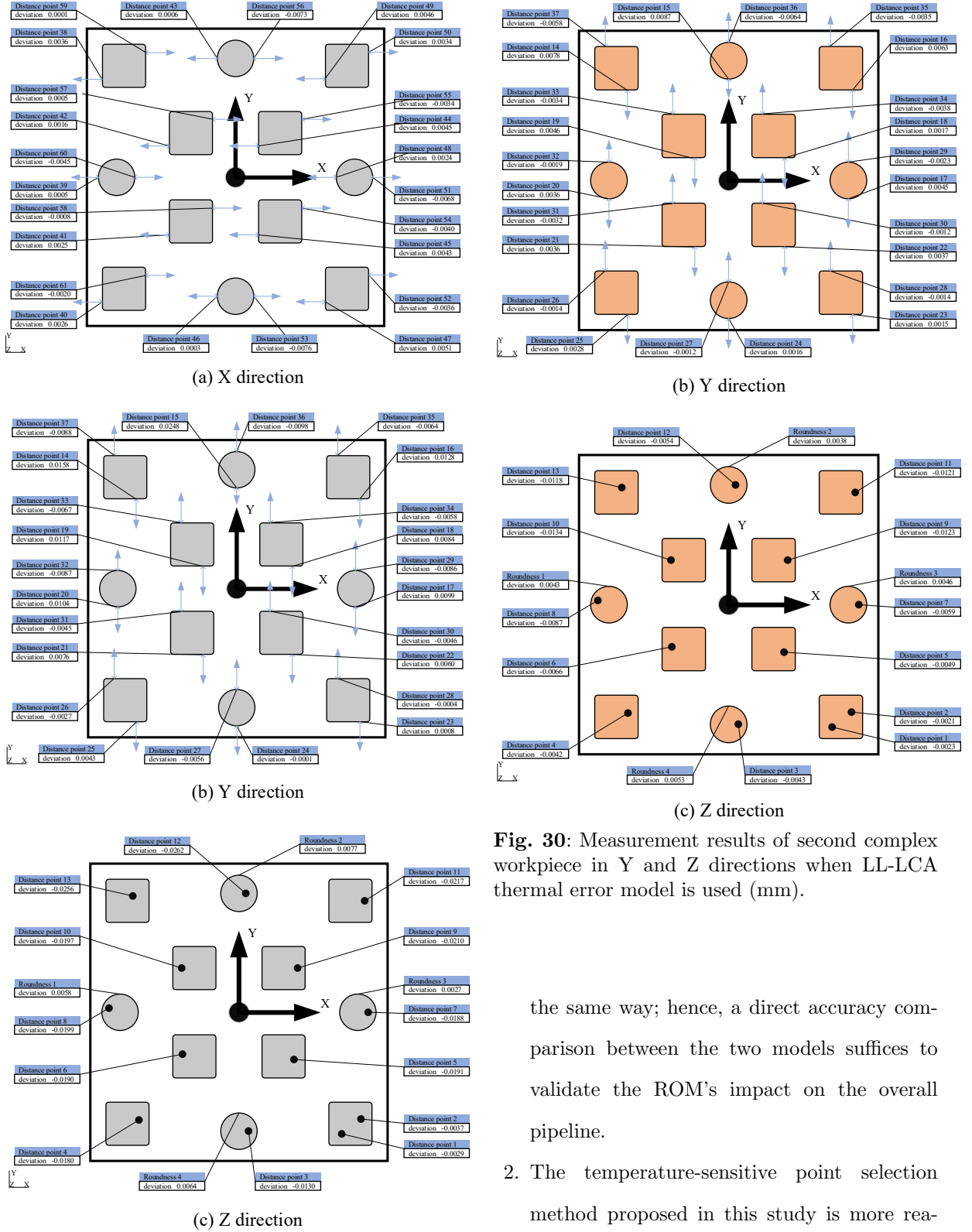


Fig. 29: Measurement results of second complex workpiece in all directions when not compensated (mm).

Fig. 30: Measurement results of second complex workpiece in Y and Z directions when LL-LCA thermal error model is used (mm).

the same way; hence, a direct accuracy comparison between the two models suffices to validate the ROM's impact on the overall pipeline.

2. The temperature-sensitive point selection method proposed in this study is more reasonable compared to directly selecting based

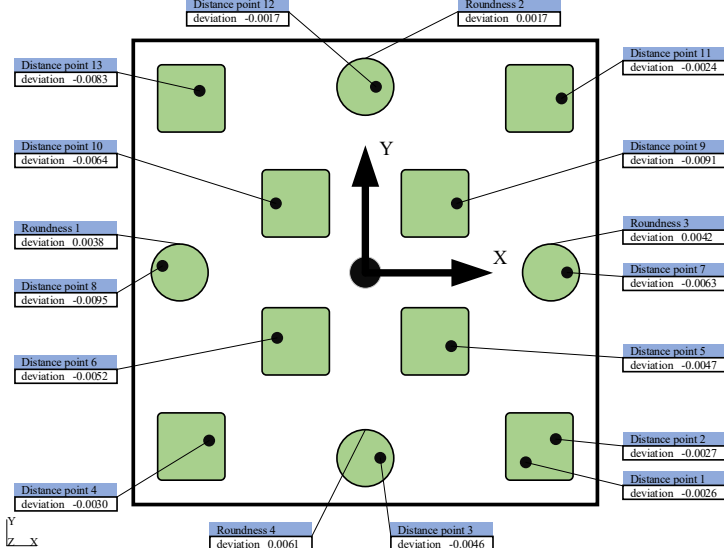


Fig. 31: Measurement results of second complex workpiece in Z direction when M-AC thermal error model is used (mm).

on the grey correlation coefficient. The simple grey correlation method is prone to being interfered by redundant temperature points. For instance, the correlations between adjacent temperature points and displacement values are both quite high, but they are redundant. *K*-means clustering can eliminate redundant points, divide key areas. Then, grey correlation selects sensitive points for each area. The combination of these two methods can improve the selection accuracy.

3. Mitigating catastrophic forgetting must be tested under conditions that mimic operational disruption. Because the data-acquisition setup used here precludes real tool changes or shutdowns, we instead vary the spindle speed to emulate the shift from roughing to finishing (Fig. 21). The results

confirm that LL-LCA retains higher prediction accuracy under these varying conditions, validating the effectiveness of the EWC regulariser.

4. In Sect. 4.3.1, T7 is employed to validate the correction method. The Z-axis ball-screw acts as an almost isolated thermal branch; hence its temperature rise is dominated by the screw's own heat input, free from cross-talk. According to Sect. 3.2.2 and Fig. 6, temperature responses T_h in (c) and (d) stem from machine-head heat-flow excitation H_h in (a) and (b). During heat-flow correction, the heat-flow–temperature paths of T1 and T6 become mutually coupled. T11 is ambient reference, leaving T7 as the cleanest indicator of pure correction performance.

5. As shown in Fig. 23 (a), after the spindle had rotated for a certain period of time, the Z-direction thermal error does not increase but decreases. Missing or mis-predicting an inflection point degrades post-compensation accuracy. Two effects are responsible: (i) The front spindle bearing carries part of the axial load at high speed, partially restraining axial thermal growth; (ii) Internal thermal coupling among spindle components and coolant flow distorts the elongation signature. These factors make purely empirical Z-axis-error models unreliable. The embedded physics-based module (PMM) captures the same physics—heat conduction and convection between components—and aggregates their deformations into net tool-tip displacement, enabling the M-AC model to locate inflection points with markedly higher fidelity.
6. DTS-TEC cuts thermal errors on both simple stepped and complex boss-shaped parts, pushing machined dimensions into the tolerance bands demanded by industry. Aerospace structural items—trusses, frame beams, seat rails—must hold linear dimensions of $\pm 0.02\text{--}\pm 0.05$ mm; after compensation, the boss workpieces produced in this study satisfy that specification, whereas the uncompensated parts do not. Likewise, 3C-mould machining for the project that motivated this work requires ≤ 20 μm error; the cutting tests confirm that DTS-TEC meets this tighter limit as well.

5 Conclusions

1. In this paper, the life-long learning method based on the EWC is applied to train the LCA network, resulting in an enhanced model adapted to varying ambient temperatures. The prediction accuracy and generalization ability of the LL-LCA network are validated using test datasets collected under varying environmental and operational conditions. An optimization method combining K -means clustering with the gray correlation coefficient is proposed to further refine selection of sensitive temperature points.
2. A M-AC thermal error prediction model is proposed, combining PMM and DDM. Through finite element transient thermal analysis of machine tool structure, the characteristics of thermal error model based on physical mechanism are obtained, which address the limitations of pure data-driven models. A heat-flow correction method using the real-time temperature data is introduced, which satisfies the thermal error compensation incorporating physical mechanisms in real-time and adaptively. The prediction effect of M-AC model is better than that of traditional thermal error model.

3. The overall framework of the DTS-TEC is proposed, enabling data accumulation and thermal error compensation. The collaborative model utilizes temperature data to calculate thermal errors in real-time. Then, DTS-TEC was implemented and deployed on the machine tool.
4. Multiple cutting experiments with varying complexities, conditions, and materials are conducted using the DTS-TEC. Results show significant improvements in machining precision, demonstrating the effectiveness of the DTS-TEC in maintaining machine tool accuracy. This construction method provides a practical and efficient approach for ensuring the thermal accuracy of machine tools.

Outlook: While the DTS-TEC significantly improves machining precision, several challenges remain. Machine tool spindle errors result from multi-factor coupling, and analyzing the coupling principles of these factors could further enhance prediction accuracy. Incorporating additional thermal boundary conditions, such as convective heat transfer inside the spindle, during the FEA simulation stage may align thermal error predictions more closely with reality. At the same time, the errors other than thermal error also need to be compensated. Developing a unified compensation model for multiple error

types is a promising future direction. For high-precision machine tools, roughing, finishing, tool changes, shutdowns, and uninterrupted processing are critical elements of real-world operations. Future research will integrate these factors into error models to further advance accuracy and robustness.

Declaration

This manuscript has not been published or presented elsewhere in part or in entirety and is not under consideration by another journal. We have read and understood your journal's policies, and we believe that neither the manuscript nor the study violates any of these.

Conflict of interest

There are no conflicts of interest to declare.

Acknowledgments

This work was supported by the Joint Funds of the National Natural Science Foundation of China (Key Program) [grant number U24A20108].

Data availability

Data will be made available on request.

References

- Dai Y, Yu B, Tao X, et al (2024) Thermal displacement prediction of variable preload motorized spindles based on speed reduction experiments and IABC-BP optimization models. Case Studies in Thermal Engineering 53. <https://doi.org/10.1016/j.csite.2023.103941>
- En-ming M, Ya-yun G, Lian-chun D, et al (2014) Temperature-sensitive point selection of thermal error model of CNC machining center. International Journal of Advanced Manufacturing Technology 74(5-8):681–691. <https://doi.org/10.1007/s00170-014-6009-y>
- Fan J, Li Z, Wang T, et al (2024) Revolutionizing gear hobbing machine precision: Innovative thermal error compensation and intelligent error control with enhanced crystal structure algorithm and self-attention bidirectional minimal gated unit network. Expert Systems with Applications 242. <https://doi.org/10.1016/j.eswa.2023.122826>
- Fan K (2017) Research on the machine tool's temperature spectrum and its application in a gear form grinding machine. International Journal of Advanced Manufacturing Technology 90(9-12):3841–3850. <https://doi.org/10.1007/s00170-016-9722-x>
- Fan K, Gao R, Zhou H, et al (2018) Study on the on-line correction of thermal parameters for machine tools. Mechanical Engineering and Technology 7(6):480–486. <https://doi.org/10.12677/MET.2018.76059>
- de Farias A, dos Santos MO, Bordinassi EC (2022) Development of a thermal error compensation system for a CNC machine using a radial basis function neural network. Journal of the Brazilian Society of Mechanical Sciences and Engineering 44(10). <https://doi.org/10.1007/s40430-022-03812-4>
- Feng Z, Min X, Jiang W, et al (2023) Study on thermal error modeling for CNC machine tools based on the improved radial basis function neural network. Applied Sciences-Basel 13(9). <https://doi.org/10.3390/app13095299>
- Fu G, Gong H, Gao H, et al (2019) Integrated thermal error modeling of machine tool spindle using a chicken swarm optimization algorithm-based radial basic function neural network. International Journal of Advanced Manufacturing Technology 105(5-6):2039–2055. <https://doi.org/10.1007/s00170-019-04388-5>
- Fu G, Tao C, Xie Y, et al (2021) Temperature-sensitive point selection for thermal error modeling of machine tool spindle by considering heat source regions. International Journal of Advanced Manufacturing Technology 105(5-6):2039–2055. <https://doi.org/10.1007/s00170-021-06608-1>

112(9-10):2447–2460. <https://doi.org/10.1007/s00170-020-06417-0>

Fu G, Zheng Y, Zhou L, et al (2023) Look-ahead prediction of spindle thermal errors with on-machine measurement and the cubic exponential smoothing-unscented kalman filtering-based temperature prediction model of the machine tools. Measurement 210. <https://doi.org/10.1016/j.measurement.2023.112536>

Li Y, Zhao J, Ji S (2018) Thermal positioning error modeling of machine tools using a bat algorithm-based back propagation neural network. International Journal of Advanced Manufacturing Technology 97(5-8):2575–2586. <https://doi.org/10.1007/s00170-018-1978-x>

Li Y, Yu M, Bai Y, et al (2021) A review of thermal error modeling methods for machine tools. Applied Sciences-Basel 11(11). <https://doi.org/10.3390/app11115216>

Li Y, Bai Y, Tian J, et al (2024) Modeling and compensation of the axial thermal error of electric spindles based on HHO-GRU method. Proceedings of the Institution of Mechanical Engineers Part B-Journal of Engineering Manufacture 238(12):1815–1826. <https://doi.org/10.1177/09544054231209786>

Liu J, Gui H, Ma C (2021a) Digital twin system of thermal error control for a large-size

gear profile grinder enabled by gated recurrent unit. Journal of Ambient Intelligence and Humanized Computing <https://doi.org/10.1007/s12652-021-03378-4>

Liu J, Ma C, Gui H, et al (2021b) Thermally-induced error compensation of spindle system based on long short term memory neural networks. Applied Soft Computing 102. <https://doi.org/10.1016/j.asoc.2021.107094>

Liu J, Ma C, Gui H, et al (2022a) Transfer learning-based thermal error prediction and control with deep residual LSTM network. Knowledge-Based Systems 237. <https://doi.org/10.1016/j.knosys.2021.107704>

Liu K, Song L, Han W, et al (2022b) Time-varying error prediction and compensation for movement axis of CNC machine tool based on digital twin. IEEE Transactions on Industrial Informatics 18(1):109–118. <https://doi.org/10.1109/TII.2021.3073649>

Liu S, Bao J, Zheng P (2023) A review of digital twin-driven machining: from digitization to intellectualization. Journal of Manufacturing Systems 67:361–378. <https://doi.org/10.1016/j.jmsy.2023.02.010>

Liu X, Masana M, Herranz L, et al (2018) Rotate your networks: better weight consolidation and less catastrophic forgetting. In:

- 2018 24th International Conference on Pattern Recognition (ICPR), Int Assoc Pattern Recognit; Chinese Assoc Automat, International Conference on Pattern Recognition, pp 2262–2268, <https://doi.org/10.1109/ICPR.2018.8545895>, 24th International Conference on Pattern Recognition (ICPR), Chinese Acad Sci, Inst Automat, Beijing, PEOPLES R CHINA, AUG 20-24, 2018
- Liu YC, Li KY, Tsai YC (2021c) Spindle thermal error prediction based on LSTM deep learning for a CNC machine tool. *Applied Sciences-Basel* 11(12). <https://doi.org/10.3390/app11125444>
- Lu C, Liu Zy, Liu Zj, et al (2015) Application of generalized radial basis function neural network to thermal error modeling. *Optics and Precision Engineering* 23(6):1705–13. <https://doi.org/10.3788/OPE.20152306.1705>
- Lu C, Fei J, Meng X, et al (2022) Thermal error prediction and compensation of digital twin laser cutting based on T-XGBoost. *Sensors* 22(18). <https://doi.org/10.3390/s22187022>
- Ma C, Gui H, Liu J (2023) Self learning-empowered thermal error control method of precision machine tools based on digital twin. *Journal of Intelligent Manufacturing* 34(2):695–717. <https://doi.org/10.1007/s10845-021-01821-z>
- Miao EM, Gong YY, Niu PC, et al (2013) Robustness of thermal error compensation modeling models of CNC machine tools. *International Journal of Advanced Manufacturing Technology* 69(9-12):2593–2603. <https://doi.org/10.1007/s00170-013-5229-x>
- Mize CD, Ziegert JC (2000) Neural network thermal error compensation of a machining center. *Precision Engineering-Journal of the International Societies for Precision Engineering and Nanotechnology* 24(4):338–346. [https://doi.org/10.1016/S0141-6359\(00\)00044-1](https://doi.org/10.1016/S0141-6359(00)00044-1)
- Ngoc HV, Mayer JRR, Bitar-Nehme E (2022) Deep learning LSTM for predicting thermally induced geometric errors using rotary axes' powers as input parameters. *Cirp Journal of Manufacturing Science and Technology* 37:70–80. <https://doi.org/10.1016/j.cirpj.2021.12.009>
- Ni J (1997) CNC machine accuracy enhancement through real-time error compensation. *Journal of Manufacturing Science and Engineering-Transactions of the ASME* 119(4B):717–725. <https://doi.org/10.1115/1.2836815>
- Niu C, Li R, Dai M, et al (2024) Research on establishment of digital-twin system for intelligent control of cutting tools sintering process driven by data-model combination. *Journal of Manufacturing Systems* 74:68–82. <https://doi.org/10.1016/j.jms.2024.01.002>

[org/10.1016/j.jmsy.2024.02.018](https://doi.org/10.1016/j.jmsy.2024.02.018)

Tan KK, Yang R, Er PV, et al (2013) RBF-based compensation method on displacement and thermal error. In: 2013 IEEE International Conference on Mechatronics and Automation, pp 1039–1044, <https://doi.org/10.1109/ICMA.2013.6618058>

Wang J, Jiang T, Shen J, et al (2020) Thermal error compensation of spindle system of computer numerically controlled machine tools through experiments and modeling. *Instrumentation, Mesure, Metrologie* 19(4):301–309. <https://doi.org/10.18280/i2m.190408>

Wu Z, Ma C, Zhang L, et al (2024) Predicting and compensating for small-sample thermal information data in precision machine tools: A spatial-temporal interactive integration network and digital twin system approach. *Applied Soft Computing* 161. <https://doi.org/10.1016/j.asoc.2024.111760>

Yang H, Ni J (2005) Dynamic neural network modeling for nonlinear, nonstationary machine tool thermally induced error. *International Journal of Machine Tools & Manufacture* 45(4-5):455–465. <https://doi.org/10.1016/j.ijmachtools.2004.09.004>

Yi H, Fan K (2023) Co-simulation-based digital twin for thermal characteristics of

motorized spindle. *International Journal of Advanced Manufacturing Technology* 125(9-10):4725–4737. <https://doi.org/10.1007/s00170-023-11060-6>

Zhang J, Li B, Zhou C, et al (2016) Positioning error prediction and compensation of ball screw feed drive system with different mounting conditions. *Proceedings of the Institution of Mechanical Engineers Part B-Journal of Engineering Manufacture* 230(12):2307–2311. <https://doi.org/10.1177/0954405416679444>

Zhang L, Ma C, Liu J (2024) Enhancing four-axis machining center accuracy through interactive fusion of spatiotemporal graph convolutional networks and an error-controlled digital twin system. *Journal of Manufacturing Processes* 112:14–31. <https://doi.org/10.1016/j.jmapro.2024.01.024>